The Cryosphere

Supplement of

Processes influencing heat transfer in the near-surface ice of Greenland's ablation zone

Benjamin H. Hills et al.

Correspondence to: Benjamin H. Hills (bhills@uw.edu)

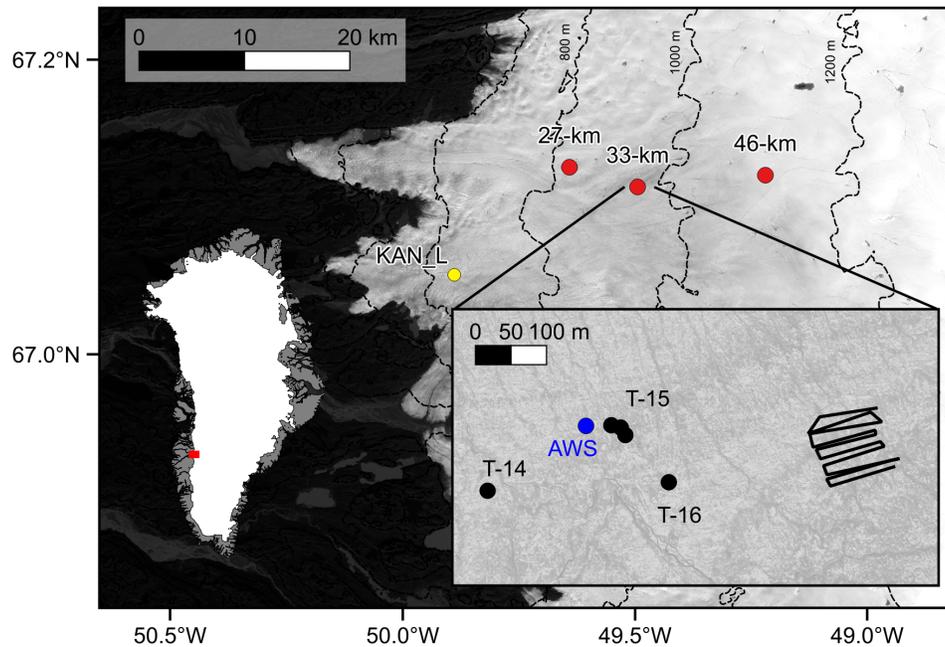# S1. Automated Weather Station

Figure S1: Same site map as Figure 1 but with an additional AWS shown at KAN_L in yellow. This station is from the Programme for Monitoring of the Greenland Ice Sheet (PROMICE) (van As et al., 2012). Ground-penetrating radar transects at the field site 33-km are shown by the black line in the inset.
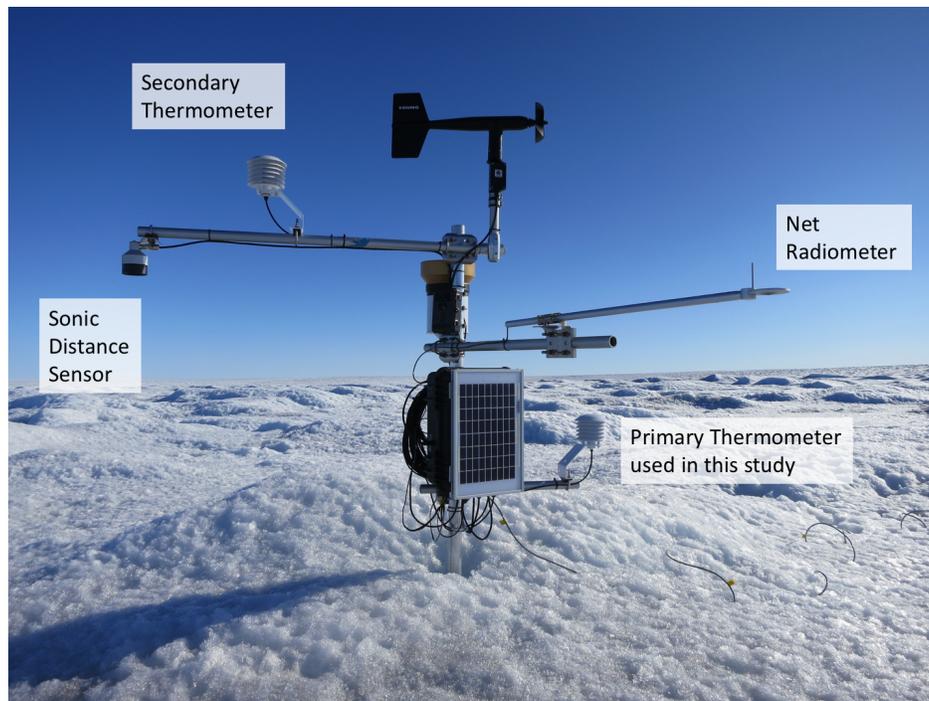

Figure S2: A photograph of the automated weather station at site 33-km, with text to indicate the relevant instrumentation used in this study.
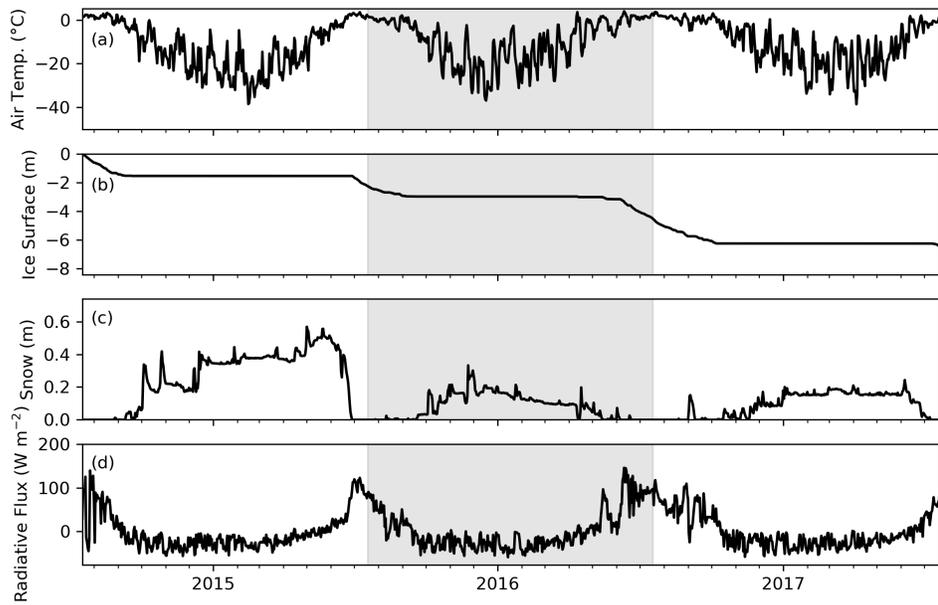
Figure S3: Meteorological data from 33-km over three years including a) air temperature, b) ice surface location, c) snow depth, and d) net radiation. All data are plotted as a daily mean. The shaded region encloses the time period that is used for the model case study in section 4.
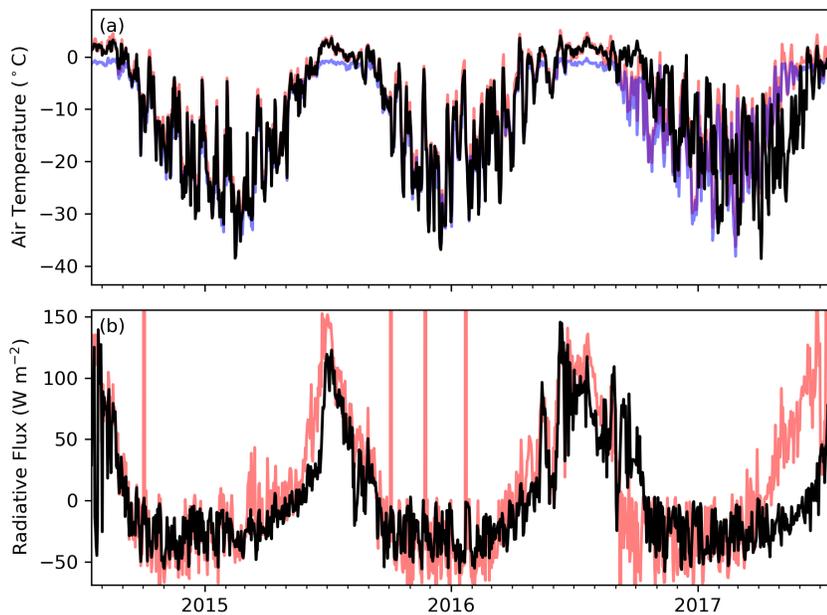

Figure S4: A comparison of the air temperature (a) and net radiation (b) measured at 33-km (black) to those at KAN_L (red). Surface ice temperature (blue) at KAN_L is calculated with the Stefan-Boltzmann Law, using the measured outgoing longwave radiation and considering ice a black body radiator. The air/ice temperatures from KAN_L are corrected for elevation with a lapse rate of -6.8°C/km (Fausto et al., 2009).

S2. Checks on Ice Temperature Measurements

In the manuscript, we define the 'depth of zero annual amplitude' as the location at which seasonal temperature oscillations are diminished to ~1%. Here, we show that this is in fact the case for the lowermost temperature sensors from each temperature string at 33-km. Figure S5 below shows the histograms and a calculated ratio of standard deviations (ice/air) over the selected time period (see Table 1). Values are within ~1% and we suspect that these calculations would be significantly smaller if the entire summer season was included (larger range for the air temperature but not necessarily for the ice temperature).
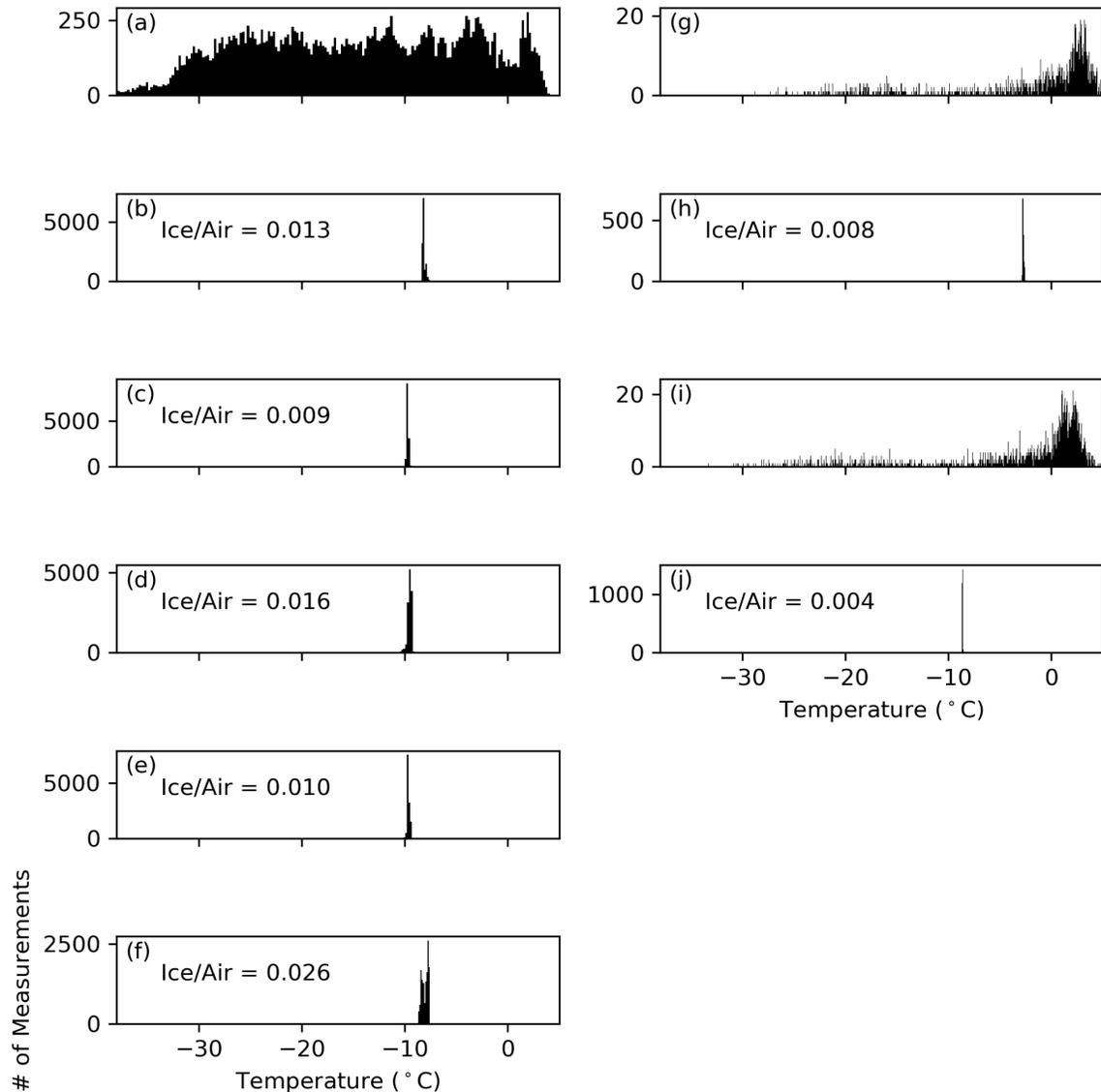

Figure S5. Histograms of measured air temperatures and ice temperatures: a) air temperature at 33-km, b) T-14, c)_T-15a, d) T-15b, e) T-15c, f) T-16, g) air temperature at 27-km, h) T-11a, i) air temperature at 46-km, j) T-11b. Temperatures presented here are from the bottommost temperature sensor on each string and from a time period over which all strings at the respective site were effectively running and collecting data (Table 1).

Thermistor measurements have a tendency to drift from the true temperature over time. To assess drift, we calculate the average difference between the measured values from string T-14 and a modeled linear fit for each measured profile (Figure S6). We use only the lowermost 10 sensors for this calculation in order to avoid most of the true transient features in the profile. This calculated drift does change in time, but it does not steadily increase or decrease. Overall, the value stays within a few tenths of a degree, giving us confidence to assert that our measurements remain robust through the entire measurement record.
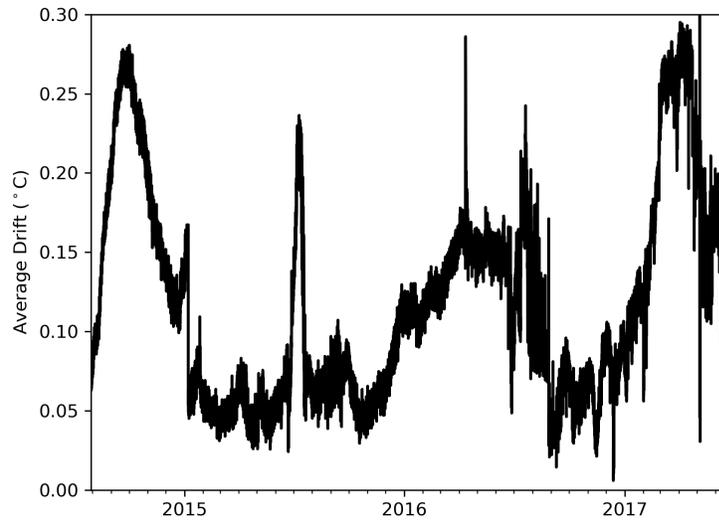

Figure S6: Calculated drift for the lowermost 10 sensors in the T-14 temperature string.

S3. Physical Evidence for Subsurface Fractures

There are no open crevasses exposed to the ice surface at the 33-km field site. However, through extensive hot-water drilling at this field location in 2014 and 2015 (Hills et al., 2017) there is substantial anecdotal evidence for subsurface fractures within the uppermost 15 m of ice (Figure S7). One form of evidence for these fractures comes during the drilling process when water in the borehole rapidly drains. Observed drainage was always in the first ~15 m of drilling (Figure S8a), and the drained water volumes are on the order of several cubic meters (Figure S8b). The total number of hot-water boreholes drilled at field site 33-km includes eleven for full-thickness instrumentation, seven for shallow temperature instrumentation, and an additional nine for video observation. Of the 27 holes, 25 separate drainage events were observed, with some holes draining more than once.
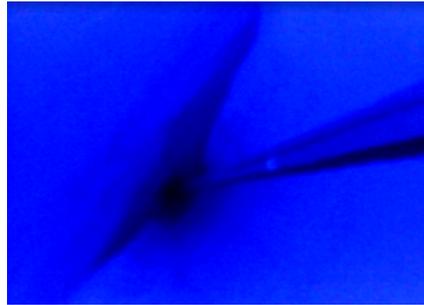

Figure S7: Photo of a subsurface fracture intersected during borehole drilling.

With borehole drainage as motivation for more subsurface investigation, a borehole video camera was used to directly observe ice below the surface. Camera observations span two different field seasons. In July of 2015, hot-water boreholes drained during drilling and dry holes (drilled with a hand-held Kovacs auger) drained if water was added. Video observations in 2015 reveal what look like subsurface fractures (Figure S7). Unfortunately the confirming images for subsurface fractures were taken after hot water drilling, so the identified features may be somewhat melted out. During a second field season in August of 2016, no hot-water holes were drilled, but many dry holes were drilled to inspect for subsurface fractures. During this season, no video observations show open features below the surface and no holes drained when water was added.
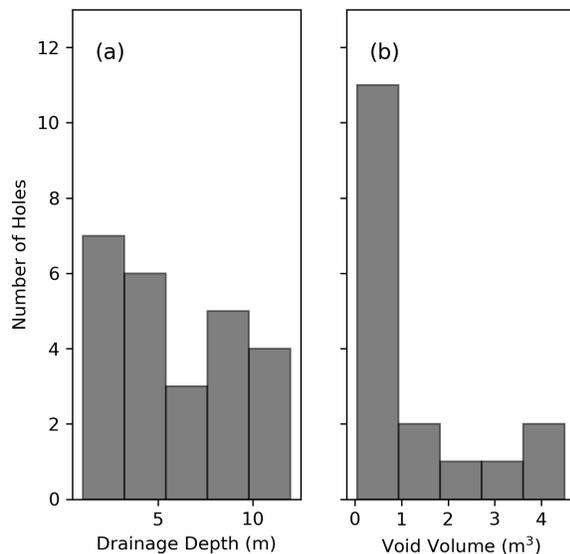

Figure S8: Drilling evidence for subsurface fractures. Histograms show the drainage depth (a) and total volume filled (b) for each of the 25 instances of drainage during hot-water drilling.

Finally, a ground-penetrating radar (GPR) survey was done to inspect ice just below the surface. This study was done with a 200-MHz shielded antenna on an SIR 3000, both from Geophysical Survey Systems Incorporated. The GPR survey consisted of 10 transects over a total of 9,000 square meters (Figure S1). Each transect is 100 m in length and separated from its neighboring transects at a common offset of 10 m. GPR data were processed with 1) a high-pass filter, 2) an exponential amplitude gain of power 1.2, 3) a 50-100-200-400 MHz bandpass filter, and 4) a horizontal demeaning filter. Among the noise caused by water and ice hummocks at the surface, the GPR data do have recognizable features which we interpret as fractures that extend 10-20 m deep. For example, one transect has a feature at 20 m horizontal distance which extends from approximately 2 to 13 m deep (Figure S9).

We now have ample evidence for subsurface fracture in the cold ice of the Greenland Ice Sheet ablation zone. In total, this evidence consists of borehole drainage in 25 separate events, video documentation after hot-water drilling, GPR reflections, and refreezing events under 5-10 m of cold ice. On the other hand, results from one season to another were not consistent. These may be transient features that open during the spring and close later in the melt season.
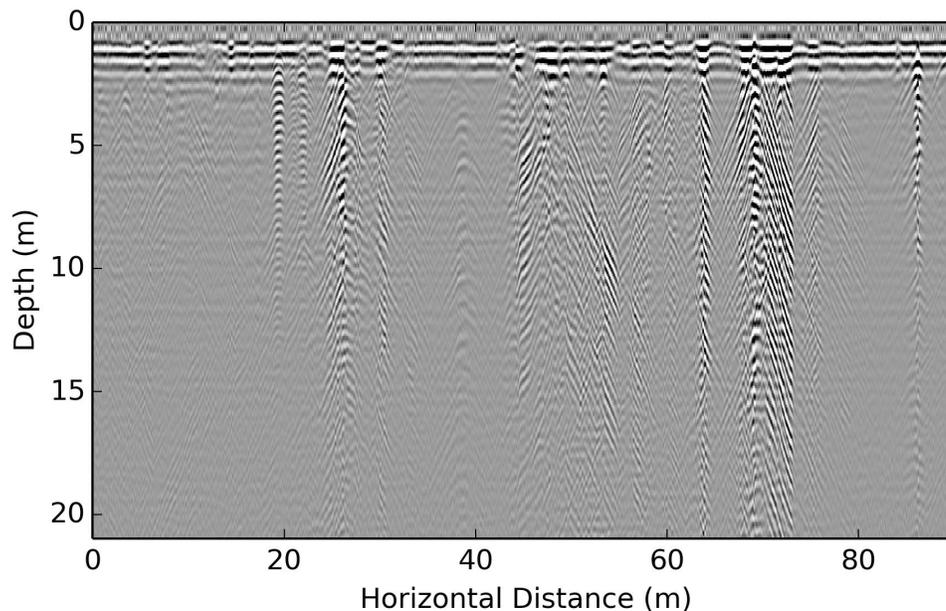

Figure S9: One transect from the ground-penetrating radar survey.

S4. Neumann Boundary Condition

In order to test the robustness of the lower boundary condition, we run a set of simulations on a 50-m model domain which correspond to the original simulations presented in the manuscript. This test was done out of concern that the Neumann boundary at the bottom of the domain could be influencing our result. We see that the larger domain has no influence on the result (with black and red lines plotting directly on top of one another).
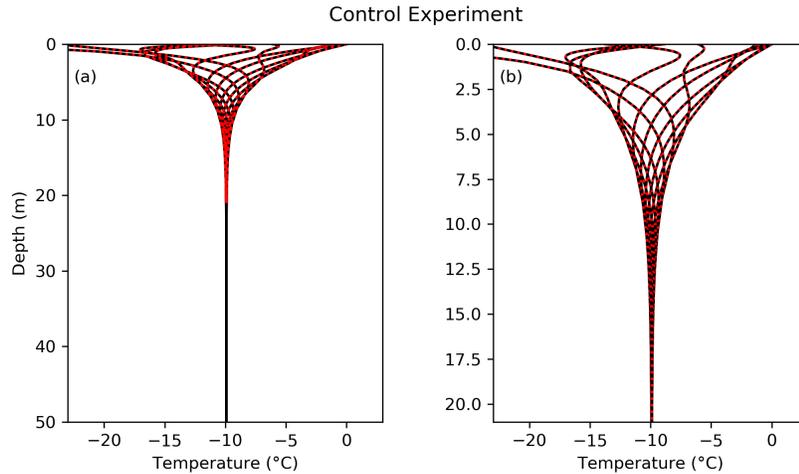

Figure S10. A comparison for the control experiment run on both a 50-m model domain (black) and on the original 21-m model domain (red dashed). Results are shown at 50 m (a) and at 21 m (b).
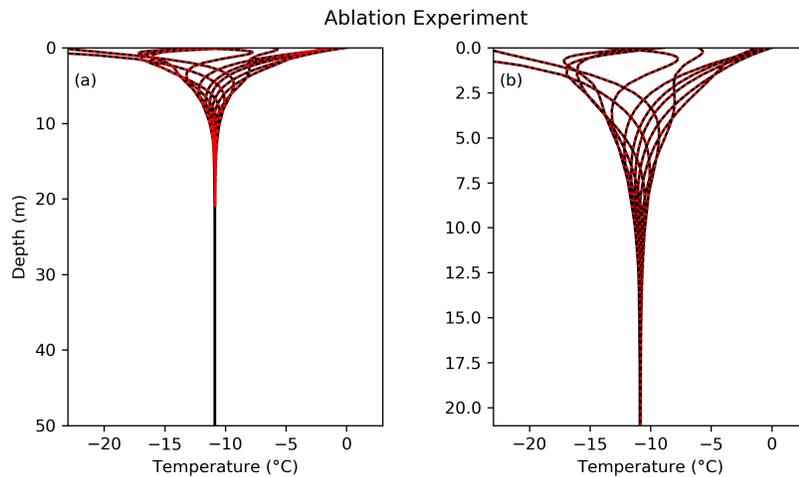

Figure S11. Same as Figure R2 except for the ablation experiment.

References

van As, D., Hubbard, A. L., Hasholt, B., Mikkelsen, A. B., van den Broeke, M. R., & Fausto, R. S. (2012). Large surface meltwater discharge from the Kangerlussuaq sector of the Greenland ice sheet during the record-warm year 2010 explained by detailed energy balance observations. *The Cryosphere*, *6*(1), 199–209. https://doi.org/10.5194/tc-6-199-2012

Fausto, R. S., Ahlstrøm, A. P., Van As, D., Bøggild, C. E., & Johnsen, S. J. (2009). A new present-day temperature parameterization for Greenland. *Journal of Glaciology*, *55*(189), 95–105. https://doi.org/10.3189/002214309788608985